Journal of Materials Chemistry A

ROYAL SOCIETY OF CHEMISTRY

PAPER

View Article Online
View Journal | View Issue

Cite this: J. Mater. Chem. A, 2026, 14, 8088

Functional off-stoichiometry in Cu(In,Ga)Se_2. Part II: electronic properties in a wide range of compositions

Kostiantyn V. Sopiha, *[a] Jan Keller, [a] Clas Persson, [b] Jonathan J. S. Scragg, [a] Charlotte Platzer-Björkman [ac] and Marika Edoff [a]

Received 29th August 2025
Accepted 9th January 2026

DOI: 10.1039/d5ta07044a

rsc.li/materials-a

Off-stoichiometry in Cu(In,Ga)Se_2 (CIGSe) is a critical material characteristic that has resisted proper understanding due to incompatible models and conflicting interpretations. In Part I of this study, we report the discovery of a topotactic transformation series of stable ordered defect compounds that properly explains the extension of the single-phase region in the phase diagram for Cu-deficient CIGSe solar absorbers. In Part II, herein, we advance this model by computing the electronic properties of all structures from the series and comparing the results with existing experimental reports. Combining the results obtained with various exchange-correlation functionals, we show monotonic band gap widening caused by the reduced p-d repulsion at the valence band edge and small dispersion of the valence band maximum for the Cu-poor structures. The small band edge dispersion is interpreted as yielding an anisotropic increase in hole mass with decreasing Cu content. These trends are consistent with prior experimental findings, giving support to the proposed model of off-stoichiometry in chalcopyrite solar energy materials.

1. Introduction

Cu(In,Ga)Se_2 (CIGSe) is an established solar absorber material for thin-film solar cells that through alloying with Ag and/or S has been proven capable of delivering power conversion efficiencies up to 23.6%.[1] The nominal chemical formula of CIGSe, however, does not convey that the absorbers are generally made Cu-poor, typically with [Cu]/[III]≡[Cu]/([In] + [Ga]) ≈ 0.85–0.95.[2] Such large off-stoichiometry is predominantly incorporated into the CIGSe grains, or more specifically into the grains of the chalcopyrite α-CIGSe phase, without segregation of secondary phases. The occasional formation of β-CIGSe (often described as Cu(In,Ga)$_3Se_5$), which occurs at greater Cu deficiencies, is practically benign. As we described in Part I, this high tolerance to off-stoichiometry originates from a topotactic transformation series – or rather, a continuum – of (near-)stable ordered defect compounds (ODCs).[3] These structures are closely related as they have a common zinc-blende parent lattice, but differ in the exact arrangement of the cations. After decades of research on unstable β-CIGSe polytypes, our discovery of this series opens new horizons for more accurate computational analysis of CIGSe in a wide range of compositions, with the possibility to replicate the actual, experimentally observed compositions in two-phase (α+β) mixtures.

Prior experimental works have already produced a deep pool of knowledge about the electronic properties of α-CIGSe and β-CIGSe phases. The most obvious difference is that undoped α-CIGSe generally shows p-type conductivity, whereas β-CIGSe is overwhelmingly identified as an n-type semiconductor,[2,4–11] with a few exceptions.[12,13] One consequence of the different conductivity types is that a p–n junction can be formed between α-CIGSe and β-CIGSe layers. In the usual case of β-CIGSe segregation due to excessive off-stoichiometry, such p–n junctions can develop sporadically throughout the absorber, inevitably impacting the device performance.

Experimentally, both phases are reported to have direct dipole-allowed band gaps, with the measured values being 0.2 ± 0.1 eV higher for the β-phase. This difference has been reproduced in first-principles calculations for CISe (*i.e.* Ga-free CIGSe) – the computed band gaps for 1 : 5 : 8 *vs.* 1 : 1 : 2 are almost universally 0.18–0.26 eV wider.[14–20] The band gap difference is not very sensitive to the structural model (see Table S1, SI) and exchange-correlation functional, which is surprising considering that all previously proposed structures for β-CIGSe are unstable to different degrees.[3] The instability does manifest itself for β-CGSe (*i.e.* In-free β-CIGSe) as its computed gaps vary greatly.[14,20,21] In extreme cases, the band gaps of α-CGSe and β-CGSe were even predicted to be identical,[14] in direct contradiction to the experimental consensus.

[a]Division of Solar Cell Technology, Department of Materials Science and Engineering, Uppsala University, Po Box 534, SE-75237 Uppsala, Sweden. E-mail: kostiantyn.sopiha@angstrom.uu.se

[b]Department of Materials Science and Engineering, KTH Royal Institute of Technology, SE-10044 Stockholm, Sweden

[c]Wallenberg Initiative Materials Science for Sustainability, Department of Materials Science and Engineering, Uppsala University, Po Box 534, SE-75237 Uppsala, Sweden

The wider gap of β-CIGSe is generally explained by a downshift of the valence band maximum (VBM), revealed both computationally[14,18,20,22] and experimentally.[4,17,23,24] These changes are associated with a reduction in Se 4p/Cu 3d antibonding at the valence band edge.[14,18,20,22] Typically, the VBM shift in computational studies is coupled with a slight downshift of the conduction band minimum (CBM), except for the band alignment computed using CdS as a common reference by Xiao and Goddard,[16] where an upshift in both the VBM and CBM was observed instead.

Another effect of Cu deficiency is on the hole mobility. Lowering the [Cu]/[III] ratio has been claimed to reduce hole mobility in epitaxial Cu-Ga-Se[25] and Se-deficient CIGSe thin films.[8] A similar effect has also been hypothesized for the Cu-In-Se system based on the hitherto available evidence.[2] This effect is principally consistent with the low dispersion (*i.e.* relative "flatness") of the band near the VBM predicted for $CuIn_5Se_8$ by Maeda *et al.*[17] Flat bands near the VBM are also recognized in computations by other authors,[14,21] albeit not universally.[21] The discrepancies in band curvature seem to stem from an inconsistent choice of structural ODC models. In contrast to holes, effective masses of electrons in the α-CISe and β-CISe phases are measured to be close,[26] in agreement with the similar band dispersions at the CBM observed in computational studies.[14,17,21]

In Part I, we demonstrated that a topotactic transformation continuum model of off-stoichiometry is highly successful in replicating the structural evolution in CIGSe with increasing Cu deficiency.[3] In Part II, herein, we validate this model for electronic properties. We perform a detailed analysis of the band gaps, densities of states (DOS), band structures, and Fermi surfaces for thirteen representative compounds with different [Cu]/[III] ratios in two ternary systems (Cu-In-Se and Cu-Ga-Se) using four different exchange-correlation functionals. These structures span the homogeneity ranges of both α-CIGSe and β-CIGSe phases, as well as the empirical miscibility gap (two-phase region) between them. Other notable low-energy structures are also studied, albeit less systematically. We reveal excellent agreement between our computational results and prior experimental findings, such as the progressive band gap widening due to the reduced p-d antibonding and low dispersion at the valence band edge in the ODCs. Quantitative matching to experimental band gaps is impressive when all necessary correlations are applied. All these results prove the great utility of the discovered stable structures for further exploration of chalcopyrite absorbers and showcase the importance of topotactic continua for understanding materials chemistry, in general.

2. Methods

2.1 Computational parameters

The first-principles calculations were performed using the Vienna *Ab initio* Simulation Package (VASP)[27] employing the projector augmented wave (PAW)[28] method within density functional theory (DFT). Four exchange-correlation functionals were extensively applied in this study: Perdew–Burke–Ernzerhof (PBE),[29] PBE with Hubbard U correction of 5 eV applied on the Cu 3d orbitals according to Dudarev *et al.* (PBE+U),[30] modified Becke–Johnson (mBJ),[31] and hybrid Heyd–Scuseria–Ernzerhof with 25% fraction of exact exchange (HSE06).[32] Occasionally, the trends were supplemented by the results obtained using the revised PBE for solids (PBEsol)[33] and strongly constrained and appropriately normed meta-GGA (SCAN)[34] functionals. Pseudopotentials with the following valence electron configurations were selected: Cu $3d^{10}4s^1$, Ga $4s^24p^1$, In $5s^25p^1$, Se $4s^24p^4$. Although the exclusion of the semicore group-III d electrons has a small effect on band edge positions,[35] it is deemed insignificant for the conclusions of this work. All structures were taken from Part I after geometry optimization, preserving the labelling.[3] Standardized primitive cells of eight selected (near-)stable structures, defined according to ref. 36, are shown in Fig. 1. In most cases, the electronic properties were computed for the structures optimized using the PBEsol functional, with several exceptions specified below. All computations were carried out using the automatically generated uniform Γ-centered k-point grids of different densities (see below) and Gaussian smearing with a 10 meV distribution width. In the case of band structure calculations, additional k-points with zero weights constituting the standard k-paths[36] were added to the automatically generated grids. Most PBE, PBEsol, and PBE+U calculations were done using a k-point density of 3000 points per reciprocal atom and a cut-off energy of 550 eV. In the HSE06 calculations, the respective parameters were reduced to 1500 points per reciprocal atom and 350 eV. For the construction of Fermi surfaces, as well as for all DOS calculations presented in the main text, the k-point grid density was drastically increased to 60 000 points per reciprocal atom, yielding much smoother iso-surfaces. All calculations were carried out in the non-spin-polarized regime because CIGSe is intrinsically non-magnetic. Spin–orbit coupling (SOC) was by default disregarded, albeit being present in chalcopyrite absorbers.[37–39] While SOC is important for accurately describing the band dispersion near split-off states, we reason that it is not essential for comparing band structures and Fermi surfaces over a large portion of the Brillouin zone. Indeed, our test calculations using the PBE+U functional confirmed this assumption, as detailed below.

2.2 Data processing

Most data processing was carried out using the pymatgen (Python Materials Genomics) library.[40] The structures were visualized using the Visualization for Electronic and STructural Analysis (VESTA) software.[41] The Fermi surfaces were visualized using the IFermi python library,[42] which relies on band interpolation by BoltzTraP2.[43] Unless specified otherwise, the reported band gaps correspond to the HSE06-computed values after an upward scissor correction of the magnitude determined below. The same adjustment was made for all band structures depicted in the main text, whereas the uncorrected results are given in the SI. All densities of states were smeared using the Gaussian function with a standard deviation of 0.02 eV.

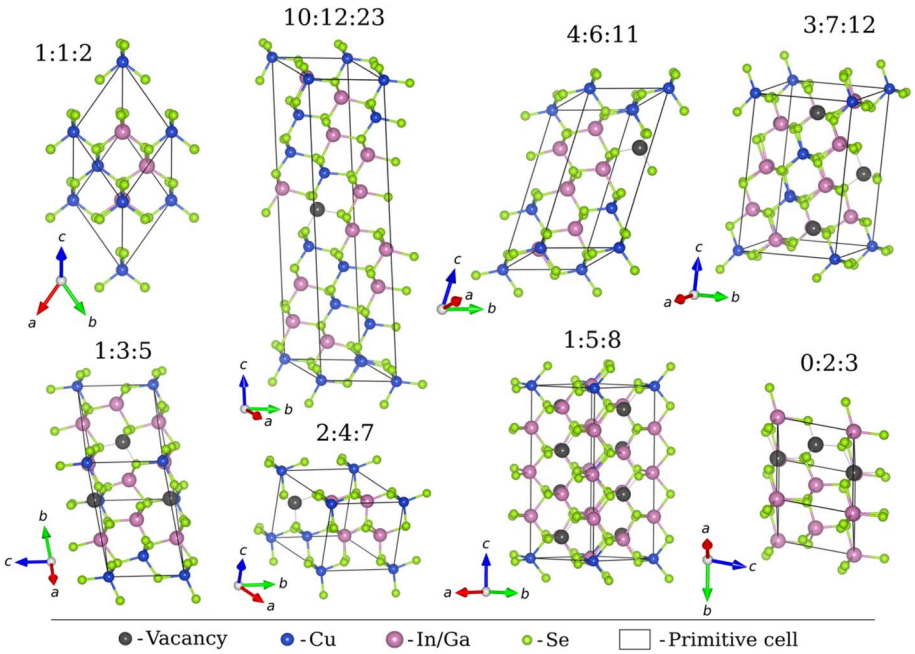

Fig. 1 Illustration of the primitive cells for eight representatives from the topotactic transformation series. All structures in the series can be accessed *via* the following identifier.[44]

3. Results

3.1 Band gap energies

We start the analysis by calculating the band gap energies of low-energy ODC structures. Fig. 2 shows the results obtained using the HSE06 and PBE+*U* functionals, alongside experimental values collected from the literature[4,5,10,12,17,24,45–61] and summarized in Table S2. All HSE06 (PBE+*U*)-computed values in this figure are scissor-corrected by +0.17 (+0.93) and +0.27 (+1.20) eV for the Cu-In-Se and Cu-Ga-Se systems, respectively. The scissor correction, which is just a constant energy shift, is applied to compensate for the well-known band gap underestimation in *ab initio* calculations.[62,63] The shift magnitudes were chosen to match the experimental band gaps reported for a wide range of compositions in both systems. The uncorrected band gaps and the effect of lattice optimization are shown in Fig. S1 and S2, SI.

Evidently, the experimental and computed gaps exhibit the same upward trend with off-stoichiometry. The computed increase in band gaps amounts to about +0.32 eV for the ground-state 1 : 5 : 8 ODCs compared with 1 : 1 : 2 chalcopyrites in both systems. Other functionals predict the band gap

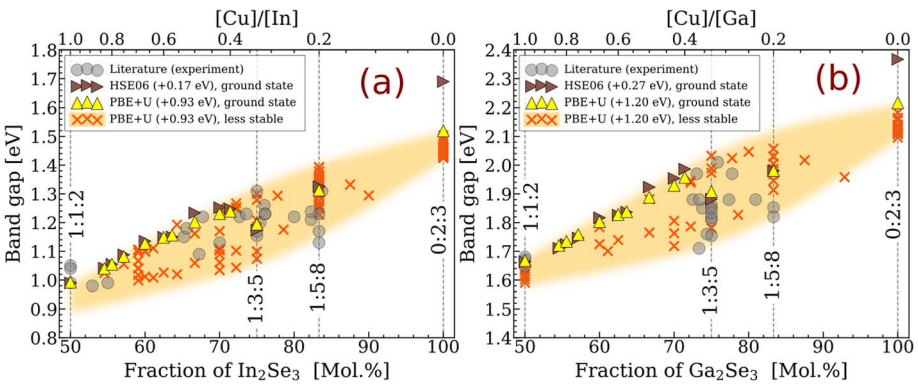

Fig. 2 Band gap energies of the low-energy structures in the (a) Cu-In-Se and (b) Cu-Ga-Se systems. The band gaps were computed using the PBE+*U* and HSE06 functionals (after geometry optimization with the respective functional) and scissor-corrected with the constant shifts specified in the legends. The term "ground state" refers to the (near-)stable structures within the topotactic series, while the term "less stable" refers to the ODC-like structures within 2.5 meV/atom of the convex hull (constructed for zinc-blende-derived structures only, *i.e.* ignoring all other polymorphs of III_2Se_3). Note that the band gaps for the less stable $CuInSe_2$ structures were excluded because many polytypes were incorrectly predicted to be metallic by the PBE+*U* functional. The experimental literature data (see Table S2) is added for comparison. The uncorrected results obtained with different functionals are given in Fig. S1.

widening too but to different extents (the gap difference for 1 : 5 : 8 *vs.* 1 : 1 : 2 varies between +0.25 and +0.52 eV, see Fig. S1). The dependence for the ground states is not monotonic though – the band gap first increases with off-stoichiometry for [Cu]/[III] $\geq$ 0.4 and then drops for the 1 : 3 : 5 ODCs. The further increase for the 1 : 5 : 8 ODCs partly offsets the drop, but the initial trend is not recovered. Although these small features are consistently predicted by different functionals (see Fig. S1), they could not be verified against experimental data because of the wide spread (about $\pm$0.1 eV) of the literature values. The main conclusion that can be drawn with such an error bar in mind is that the general band gap widening trend is successfully reproduced.

A possible reason behind the wide spread of experimental band gaps is the formation of different polytypes, originating from variations in processing conditions. To estimate the potential electronic impact of the polymorphism, the band gap energies were also computed for the ODC-like structures within 2.5 meV/atom of the convex hull.[3] The values obtained with the PBE+*U* functional after the scissor correction are presented in Fig. 2 as "less stable" structures. As one can see, most added datapoints are below the band gaps (for the ground states in the 0.4 $\leq$ [Cu]/[III] $\leq$ 1.0 range) or scattered around them (for the 1 : 3 : 5 and 1 : 5 : 8 ODCs). Curiously, the highest computed gaps exhibit a linear dependence on the III_2Se_3 fraction. After including the "less stable" structures, the spread of the computed gaps is about $\pm$0.1 eV, which is the same as for the measured values, suggesting that polymorphism can fully account for the experimental band gap variations.

The effect of polymorphism on the band gap for ODCs is comparable in magnitude to that observed for the 1 : 1 : 2 polytypes formed by intermixing chalcopyrite-like (CH-type) and CuAu-like (CA-type) layers.[3,64] As illustrated in Fig. S3a, the band gaps decrease linearly with the CA-type fraction, amounting to the reductions of 0.12 eV for $CuInSe_2$ and 0.40 eV for $CuGaSe_2$. Since the polytype formation enthalpies also vary linearly with the CA-type fraction,[3,64] a linear correlation between the band gaps and formation enthalpies was anticipated. This hypothesis is validated in Fig. S3b, which further reveals that the rates of the band gap change with the polytype formation enthalpy for $CuInSe_2$ and $CuGaSe_2$ are comparable, in agreement with prior findings for sulfide chalcopyrites.[65] Under the chosen energy threshold of 2.5 meV/atom for the "less stable" structures, these linear trends yield similar band gap spreads at [Cu]/[III] = 1 for both systems in Fig. 2.

The linear correlation between the band gaps and the formation enthalpies does not hold for the ODC polytypes. As shown in Fig. S4, which is based on the high-throughput screening from Part I,[3] the band gaps are generally slightly lower for less stable 1 : 5 : 8 polytypes, but the correlation is very loose. As such, we conclude that structural instability is not the main factor modulating the electronic properties of the ODCs.

Noting the spread of band gaps for different polytypes, a question arises about the magnitude of errors in the literature due to the use of unstable ODC structures. To estimate them, we calculated band gaps for a collection of structures compiled from different publications[14–19,21,66–77] and databases[78–80] using the PBE+*U* functional, and summarized in Table S1. Evidently, most literature structures substantially underestimate the band gap changes with off-stoichiometry in CIGSe. For the most frequently used ODC structures (so-called "Type-D" and "Type-E"), the PBE+*U*-computed values are augmented with calculations using the HSE06 functional and two Ag-containing systems (Ag-In-Se and Ag-Ga-Se), and summarized in Table 1. As one can see, the "Type-E" structures of $CuIn_5Se_8$ and $CuGa_5Se_8$ have HSE06-computed gaps 0.25 and 0.07 eV higher than the respective 1 : 1 : 2 chalcopyrites. These values constitute an underestimation of the band gaps by 0.08 and 0.25 eV compared with the ground states. The difference is even greater for $AgIn_5Se_8$ and $AgGa_5Se_8$. Crucially, these band gap errors almost completely (for $AgGa_5Se_8$), drastically (for $CuGa_5Se_8$), or partly (for $CuIn_5Se_8$ and $AgIn_5Se_8$) offset the effect of off-stoichiometry, thereby undermining all conclusions derived for the "Type-E" structures in prior studies. The most stable literature alternative, namely the "Type-D" structure, can only further exacerbate the problem, to the extent that the computed band gap decreases for 1 : 5 : 8 ODC compared with the 1 : 1 : 2 chalcopyrite in the Cu-Ga-Se and Ag-Ga-Se systems. For reference, our prior spectrophotometric measurements for co-evaporated Ag-Ga-Se films with various compositions have shown about 0.33 eV wider band gap for $AgGa_5Se_8$ ($E_g = 2.11$ eV) than $AgGaSe_2$ ($E_g = 1.78$ eV),[81] in good agreement with our calculations for the ground state structures (see Table 1). Hence, it is of paramount importance to critically rethink the ODCs for the entire I-III-VI material family by scrutinizing true ground states and other low-energy polytypes studied herein.

3.2 Densities of states

The band gap widening effect of off-stoichiometry in CIGSe is usually explained by reduced antibonding in the valence band. Fig. 3a illustrates the orbital hybridization scheme for chalcopyrites.[82–85] Here, the renowned antibonding nature of the valence band top – highly consequential for the defect tolerance of CIGSe (see Zakutayev *et al.*[86]) – is shown to originate from the hybridization of Se 4p and Cu 3d orbitals. Note that the antibonding and bonding parts of the valence band are separated by a repulsion gap.[18,20]

To assess how orbital hybridization evolves across the topotactic continuum in CIGSe, element-projected densities of states (DOS) were computed for the (near-)stable structures with the geometries optimized using the PBEsol functional. Fig. 3b and c illustrate the results of mBJ calculations augmented by the scissor correction of band gaps to match the corrected HSE06-computed values (as in Fig. 2). The uncorrected DOS obtained with different functionals for a slightly wider ODC series are presented in Fig. S5 and S6.

As evident from Fig. 3, the p-d antibonding is confirmed to generate a repulsion gap for the 1 : 1 : 2 stoichiometry. This gap in the valence band is not directly linked to the macroscopic material properties, but the way it evolves with off-stoichiometry is emblematic of the varying electronic structure. The states above the repulsion gap are dominated by Cu 3d orbitals, with minor contributions from the other elements, as expected in the

Table 1 The computed difference in band gaps of the 1 : 5 : 8 ODC and 1 : 1 : 2 chalcopyrite structures in different I-III-VI systems. The results were obtained using the PBE+*U* (without parentheses) and HSE06 (within parentheses) functionals. The pseudopotential of Ag with the $4d^{10}5s^{1}$ valence electron configuration was adopted and Hubbard *U* correction of 5 eV was applied on Ag 4d orbitals in the PBE+*U* calculations. All geometries were fully reoptimized

Compound	Ground state (ref. 3)	"Type-E" (ref. 14, 17, 19, 67, 70, 72 and 77)	"Type-D" (ref. 15, 16, 18, 66, 67, 70 and 73–76)
$CuIn_5Se_8$	+0.32 (+0.33)	+0.25 (+0.25)	+0.24 (+0.24)
$CuGa_5Se_8$	+0.31 (+0.32)	+0.12 (+0.07)	+0.02 (−0.07)
$AgIn_5Se_8$	+0.29 (+0.38)	+0.21 (+0.29)	+0.09 (+0.14)
$AgGa_5Se_8$	+0.30 (+0.37)	−0.01 (+0.02)	−0.18 (−0.21)

case of antibonding. The states right below the repulsion gap have sizable contributions from all elements, which is typical of chemical bonding. The repulsion gaps here extend from −3.98 to −2.82 eV for $CuInSe_2$ and between −4.84 and −3.59 eV for $CuGaSe_2$ (all energies are given relative to the CBM), meaning that their magnitudes (1.16 and 1.25 eV, respectively) are significantly overestimated compared to the literature values of 0.2–0.3 eV for $CuInSe_2$ computed within the local density approximation (LDA)[18] and hybrid HSE[20] functionals. As shown in Fig. S5 and S6, this discrepancy is consistent across the board and is fully explained by the mBJ functional yielding overly localized (less hybridized) states. For reference, the repulsion gap widths computed with the PBE (HSE06) functional are 0.63 (0.20) eV for $CuInSe_2$ and 0.73 (0.35) eV for $CuGaSe_2$, whereas the PBE+*U* functional predicts nearly zero repulsion gaps of 0.02 and 0.10 eV, respectively. Computationally, this result demonstrates that the band gap enhancement delivered by the mBJ functional comes at the cost of the less accurate description of hybridization within the bands. However, this artifact is handy in our case because it highlights the key differences between the ODCs within the topotactic series.

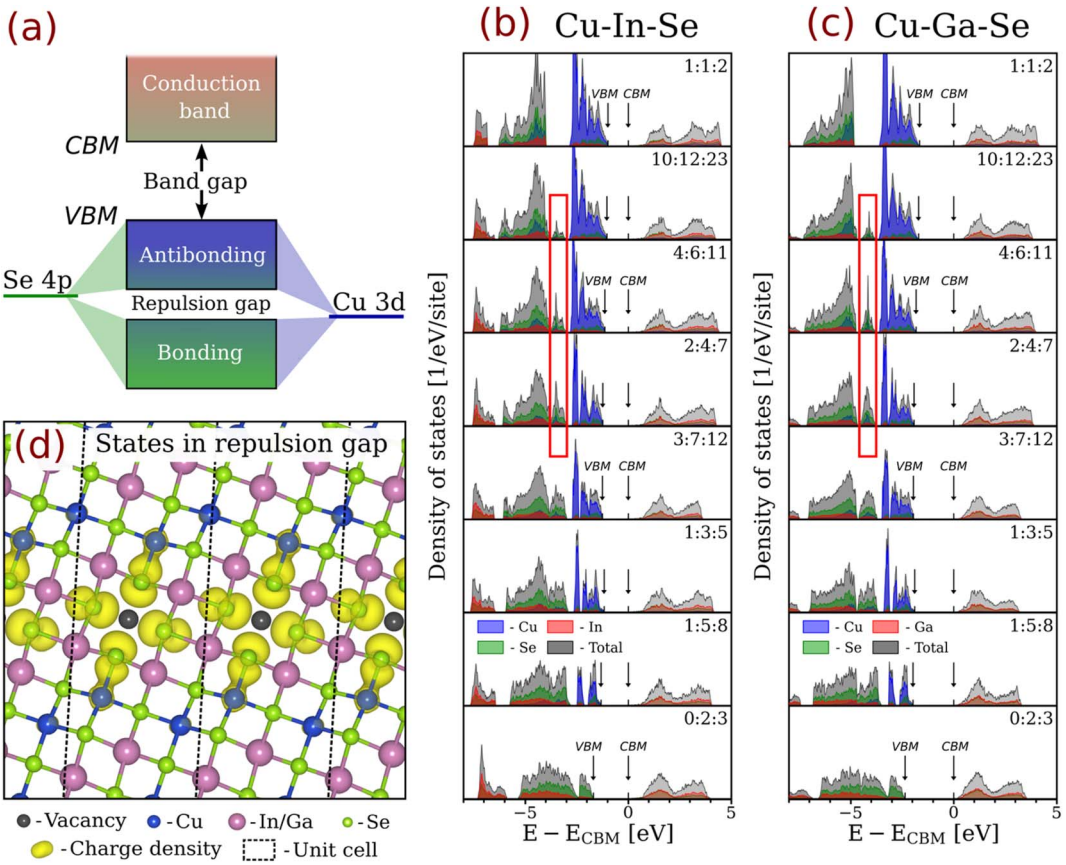

Fig. 3 (a) Schematic of the orbital hybridization at the band edges in chalcopyrites. Element-projected densities of states computed using the mBJ functional for different (near-)stable structures in the (b) Cu-In-Se and (c) Cu-Ga-Se systems. (d) Charge density distribution for the states emerging in the repulsion gap for the ODCs as computed for $Cu_{10}In_{12}Se_{23}$ using the mBJ functional (the isosurface is at 0.01 e/a_0^3, where a_0 is the Bohr radius). The states in question are outlined by the red rectangles in (b) and (c). The band gaps here are adjusted to the scissor-corrected HSE06 values shown in Fig. 2. The uncorrected densities of states for a slightly extended ODC series computed using other functionals are presented in Fig. S5 and S6.

The most notable difference in the electronic structures within the topotactic series occurs in the valence band, whereas the conduction band undergoes only subtle changes. This is expected because the decrease in the fraction of Cu ions means fewer Cu 3d orbitals in the valence band. Consequently, the density of states and the width of the antibonding band decrease.[87] The Se 4p orbitals, which contribute to Cu–Se bonds in 1 : 1 : 2 chalcopyrites, hybridize with In 5p (or Ga 4p) orbitals in the ODCs instead, forming In–Se (or Ga–Se) bonds with the state densities in the repulsion gap. These states have energies higher than the other In–Se (or Ga–Se) bonds because they localize on the undercoordinated Se atoms adjacent to vacancies, as evident from the state-projected charge density in Fig. 3d. Upon lowering the [Cu]/[III] ratio, ever more states emerge in the repulsion gap at the expense of reduced antibonding. This evolution is gradual and it culminates in a complete removal of the antibonding band for the most stable zinc-blende-derived 0 : 2 : 3 structures in both systems.

The fact that the antibonding states in the valence band gradually fade away as the Cu deficiency increases implies that the band gap widening in the ODCs is primarily caused by a downshift of the valence band edge. In this case, the electronic contributions of [Cu]/[III] changes must be decoupled from those of Ga alloying, as suggested by Stokes *et al.*,[88] because the addition of Ga mostly affects the conduction band edge.[89,90] Work is ongoing to validate this conclusion with new interface models based on the stable ODC structures and more rigorous computational procedures.

3.3 Band structures

To further explore the nature of electronic structure changes across the topotactic ODC series, we computed the element-projected band structures for the entire series using different functionals. Fig. 4 shows the results obtained with the mBJ functional for selected compositions in the Cu-In-Se system. Here too the PBEsol-optimized geometries were used and the band gaps were adjusted to the corrected HSE06-computed values (as in Fig. 2). The uncorrected band structures obtained with other functionals for a wider ODC series are presented in Fig. S7–S14. Clearly, among all studied functionals, mBJ consistently yields the smallest band dispersion (*i.e.* the flattest bands) due to the excessive orbital localization, in line with prior observations.[91,92] The excessive localization is evident for Cu 3d orbitals, which give the deep blue color to the element-projected valence bands in our mBJ calculations, in contrast to the more mixed orbital contributions to the valence band predicted by all other functionals. The difference in band dispersion is best illustrated in Fig. S15 and S16, where band structures obtained with different functionals are compared after scissor-correcting the computed band gaps. The effect of SOC is shown using the PBE+*U* functional in Fig. S17 and S18. Clearly, SOC slightly modifies the valence band edge at the Γ point, but all key features of the band structures are preserved. This result justifies our decision to neglect SOC in most calculations presented herein.

Akin to the 1 : 1 : 2 chalcopyrites, all ODCs are seen to have direct (or near-direct) band gaps at the Γ point, in agreement with optical absorption measurements.[7,48,50,93–95] This result is also consistent with prior computational studies of unstable 1 : 3 : 5 and 1 : 5 : 8 ODC structures, which always report direct band gaps at the Γ point in both the Cu-In-Se and Cu-Ga-Se systems.[14,17,21] The conduction bands for the ODC structures do not exhibit stark differences, whereas the valence band evolves such that the bands near the VBM become relatively flat along one of the segments (Z-Γ, X-Γ, or M-Γ). In real space, these segments align with different crystallographic axes of the parent chalcopyrite lattice, notably $[041]_{CH}$ for structures with 0.5 < [Cu]/[In] < 1.0, and $[\bar{1}10]_{CH}$ for the 1 : 3 : 5 and 1 : 5 : 8 ODCs (see Fig. S19). The flatness is greater in the Cu-In-Se system than in the Cu-Ga-Se system, regardless of the functional. It should be reiterated, however, that the mBJ functional used to produce Fig. 4 exaggerates band flatness, rendering the magnitude of the effect unreliable, but the qualitative shift towards heavier holes is robust.

Flat bands near the VBM have already been noted by Maeda *et al.*[17] and can also be recognized in other studies of the "Type-A" and "Type-E" 1 : 5 : 8 ODCs.[14,21] However, no flat bands can be seen for the 1 : 3 : 5 ODC and 1 : 5 : 8 ODC with the space group *C*222 reported by Liu *et al.*[21] To investigate the propensity for the flat band edge character among the ODC polytypes, we computed (using the PBE+*U* functional) the band structures of nine literature 1 : 5 : 8 structures listed in Table S1. To facilitate comparison, the calculations were performed for unit cells with identical geometries (aside from minor structural relaxations), allowing the use of a consistent *k*-path irrespective of formal symmetry. The results in Fig. S20 and S21 reveal that the valence band edge dispersion varies substantially among the 1 : 5 : 8 polytypes, yet most valence band edge curvatures are smaller compared with the chalcopyrite reference along the X-Γ and/or Y-Γ segments (corresponding to the $[1\bar{1}0]_{CH}$ and/or $[110]_{CH}$ axes in real space). This finding highlights the high sensitivity of the β-CIGSe electronic properties to cationic arrangements, with a general tendency toward band flattening. This conclusion is reinforced by the band structures computed for the slightly less stable 1 : 5 : 8 ODC structure in Fig. S7–S14. Despite only 0.02 and 0.6 meV/atom higher enthalpy than the ground state in the Cu-In-Se and Cu-Ga-Se systems, respectively (according to the PBE results),[3] the difference in band dispersion is apparent. Hence, further calculations of electronic properties should be performed on ensembles of low-energy structures to replicate the partial cationic disorder in real ODC materials.

For the structures in the 0.5 < [Cu]/[III] < 1.0 range, where multiple low-energy structural polytypes can be formed by varying the separation between the Cu-poor regions,[3] the valence band dispersion can be analyzed as a function of the separation pattern. To probe the dependence, we computed the band structures for two 4 : 6 : 11 ODC polytypes and performed band unfolding (using the easyunfold package)[96] with the most stable polytype serving as the primitive cell. The results in Fig. S22 illustrate that the band flattening effect is enhanced for the irregular separation between the Cu-poor regions, presumably due to broken symmetry in the perpendicular direction.

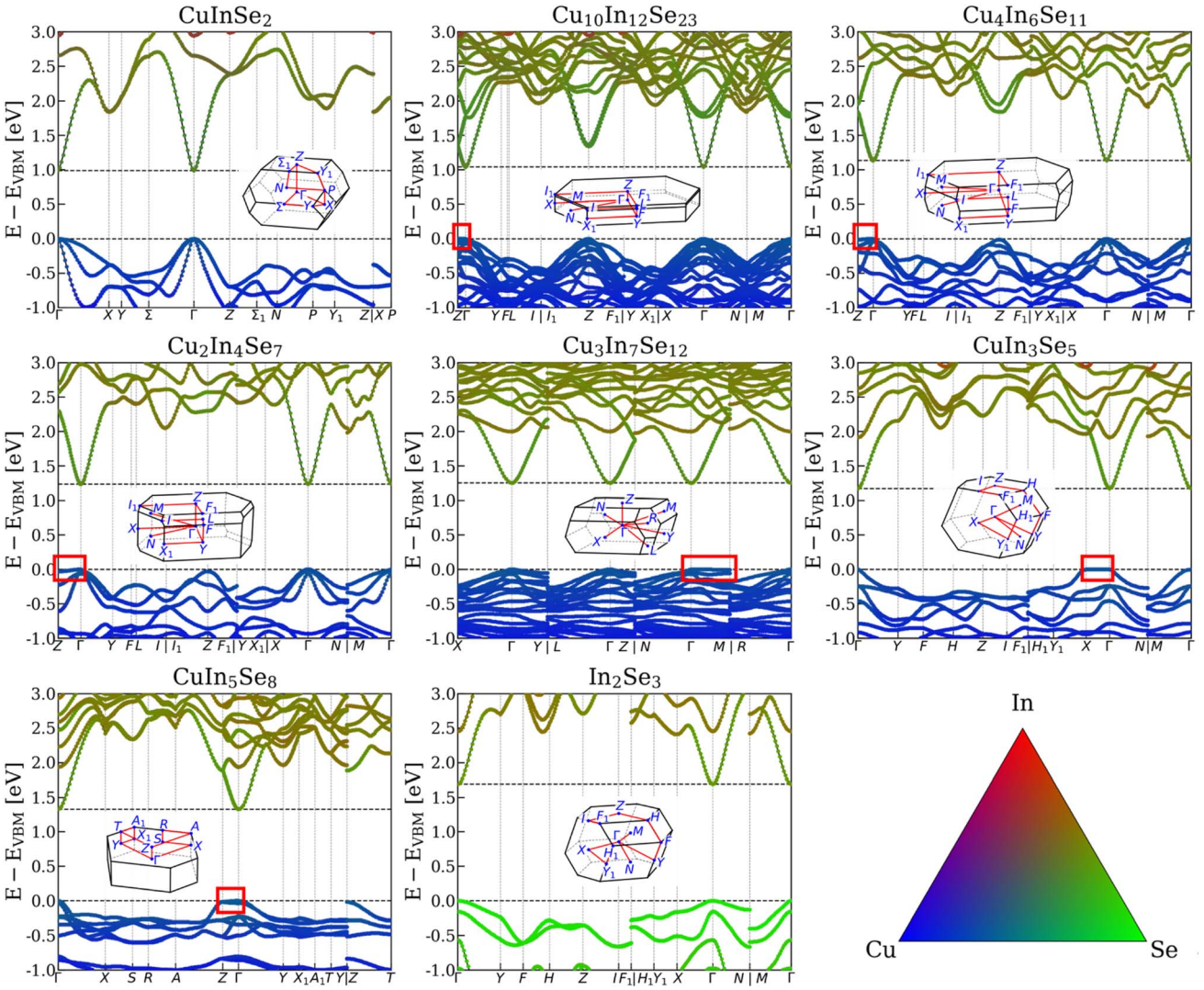

Fig. 4 Element-projected band structures of selected structures within the topotactic transformation series computed using the mBJ functional for the Cu-In-Se system. The band gaps here are adjusted to the scissor-corrected HSE06-computed values shown in Fig. 2. The flat bands near the VBM are outlined by the red rectangles. The insets illustrate the Brillouin zones. The color triangle encodes the orbital contributions. The uncorrected band structures for the entire series in both the Cu-In-Se and Cu-Ga-Se systems computed with the mBJ, PBE, PBE+*U*, and HSE06 functionals are presented in Fig. S7–S14.

This result implies that dispersion of the valence band in α-CIGSe is likely to decrease with cationic disorder, which is expected to manifest as random separation between the Cu-poor regions already at room temperature.[3]

3.4 Fermi surfaces

The curvature of a band $E(k)$ is often described by the effective mass along a given k-vector as $m^* = \left(\frac{1}{\hbar^2}\frac{d^2E}{dk^2}\right)^{-1}$. However, this quantity is characteristic of a specific k-point and does not account for non-parabolicity or anisotropy of the band over a large k-space region. This constitutes a problem for the ODCs, which exhibit very complex dispersions of the uppermost valence band, with a relatively flat segment near the band edge (see Fig. 4). As a result, holes in the ODCs must occupy regions of the band characterized by different effective masses. To avoid the undue complexity, we herein discuss the changes in the carrier masses qualitatively based on the band curvatures and Fermi surfaces (*i.e.* constant energy surfaces) plotted for bands at 26 meV ($\approx 1\ k_BT$) below the VBM and 0.13 eV ($\approx 5\ k_BT$) above the CBM. The Fermi surfaces from the mBJ calculations for four stable structures in the series are given in Fig. 5. The results computed with the mBJ and PBE+*U* functionals are shown in Fig. S23–S26.

For all structures in the series, the Fermi surfaces at the CBM appear as ellipsoidal pockets with low eccentricity (see Fig. 5), meaning that the electron mass is marginally anisotropic (as noted computationally for stoichiometric α-CIGSe in ref. 37–39 and confirmed experimentally in ref. 97 and 98). As the shape is unaffected by the changing [Cu]/[III], the electron mass is roughly constant, in agreement with earlier measurements of similar electron effective masses in α-CISe and β-CISe.[26]

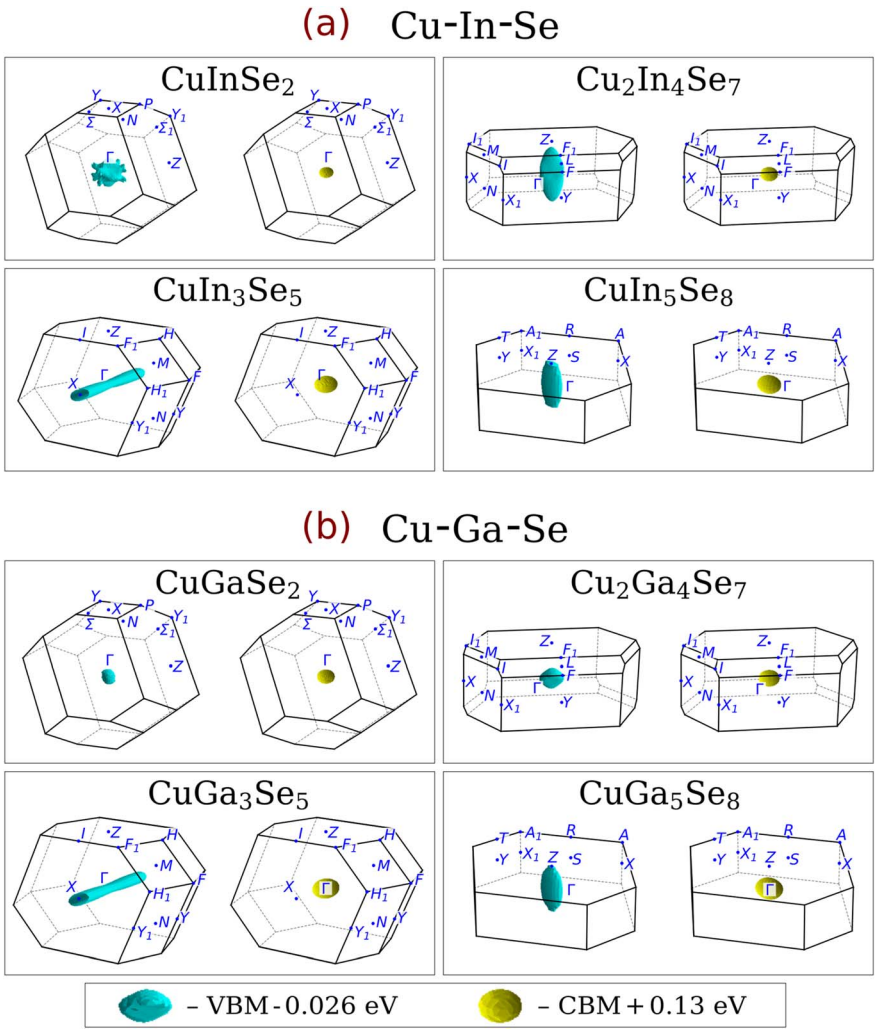

Fig. 5 Fermi surfaces in the Brillouin zones of four stable structures in the (a) Cu-In-Se and (b) Cu-Ga-Se systems computed with the mBJ functional and constructed at energies 26 meV below the VBM and 130 meV above the CBM. The Brillouin zones are shown with differing scales across the structures. The corresponding Fermi surfaces obtained with the PBE+*U* and mBJ functionals for other (near-)stable structures in the series are illustrated in Fig. S23–S26.

In contrast, the hole mass increases for Cu-poor CIGSe as the Fermi surfaces elongate along the *k*-direction of the flat band near the VBM. In real space, this situation describes impeded hole transport across the Cu-poor regions (see Fig. S19), which is intuitively understood: reduced antibonding lowers the VBM level near the vacancies, creating local potential barriers for holes. A similar mechanism is often applied to describe contributions from Cu-poor grain boundaries,[99] and it is in line with the drop in carrier mobility measured for Cu-poor α-CGSe[25] and Se-deficient α-CIGSe[8] absorbers. The predicted transport anisotropy is especially strong for the 1 : 3 : 5 and "less-stable" 1 : 5 : 8 ODCs, which exhibit Fermi surfaces of nearly cylindrical shape, closely resembling those of isotropic 2D materials.[100] Anisotropic Fermi surfaces at the valence band edge are also observed in most literature 1 : 5 : 8 polytypes (see Fig. S20 and S21), with the hole mass being the largest along the $[1\bar{1}0]_{CH}$ and/or $[110]_{CH}$ directions, in line with the results for the ground-state and the slightly less stable 1 : 5 : 8 structures. Notably, the Fermi surface shapes vary considerably among the polytypes, suggesting that hole mobility in β-CIGSe is sensitive to the cationic arrangement.

4. Discussion

The computed band gap widening with off-stoichiometry across the topotactic series has several experimental manifestations. In homogeneous Cu-poor CIGSe powders, variations in the [I]/[III] ratio have been reported to gradually blueshift the absorption edge.[17] As confirmed here, the band gap widening originates from reduced Cu 3d/Se 4p antibonding and is thus likely dominated by a downshift of the valence band edge, consistent with experimental observations.[4,23] The resulting band alignment between the distinct CIGSe phases can therefore introduce a hole transport barrier. Such a barrier may enhance photocarrier collection when β-CIGSe occurs as a thin Cu-deficient layer at the absorber/buffer interface,[14,101–103] but it

can also block photocurrent when β-CIGSe segregates at the back contact, as observed in Ag-alloyed CIGSe.[104–106] Moreover, because β-CIGSe exhibits n-type conductivity,[2,4–11] a charge-depletion region can develop at its interface with p-type α-CIGSe.[4] On the one hand, this depletion contributes to the beneficial "buried homojunction" formation,[103,107] but on the other hand it may be detrimental if β-CIGSe grains (and hence local charge depletion) occur sporadically throughout the absorber. In practice, however, mixed phase morphology is not always an issue, considering that even a substantial β-CIGSe presence exerts surprisingly little influence on solar cell performance,[108–112] indicating that the α-CIGSe/β-CIGSe junction remains insufficiently understood. Furthermore, it has been demonstrated that β-CIGSe can yield functioning solar cells with power conversion efficiencies above 14% in the standard CIGSe solar cell architecture.[113] A possible explanation for the realization of a working device from a stack that should lack a p–n junction is that certain impurities (*e.g.* Na and/or Cd) converted the β-CIGSe film into a p-type semiconductor. It remains unclear whether such conductivity type inversion is operative in these systems, but it would help reconcile the observations from the material- and device-oriented studies.

Interfacial band offsets in CIGSe solar cells have already been studied computationally,[14,16,18,22] but all prior works relied on unstable 1 : 5 : 8 ODC polytypes. While they did confirm that a large contribution comes from the VBM downshift, the quantitative errors of at least 0.1–0.3 eV due to the band gap underestimation owing to the use of unstable structures cast doubt on the numerical results. These computational errors, compounded by the variability of experimental data, underscore the need for a systematic revision of interfacial band alignment in two-phase CIGSe absorbers. Such a revision should employ more representative interface models grounded in the structural motif of the topotactic series. The prospect of improvement is especially bright for heavily Ag-alloyed CIGSe absorbers, which, on the one hand, are particularly prone to segregation of the β-phase,[104,105,114] while on the other hand, have the band gaps most severely impacted by the instability of literature structures, as evident from our calculations for the Ag-Ga-Se system.

The minimal variation in the electron effective mass across the topotactic series, as inferred from the computed band structures and Fermi surfaces, is reminiscent of the predictions put forward in ref. 115. In that work, off-stoichiometry in CIGSe was hypothesised to be mediated by superclusters formed through the aggregation of charged point defects. Such superclusters were proposed to be overall neutral and dipole-free; however, the constituent negatively charged vacancies were suggested to repel free electrons, thereby minimizing electron-defect interactions. In contrast, within the topotactic continuum model, the Cu-poor regions that accommodate off-stoichiometry in α-CIGSe do not arise from defect clustering,[3] yet their impact on free electrons is likewise minimal, as evidenced by the invariance of the electron effective mass with respect to the [Cu]/[III] ratio. From this perspective, the topotactic continuum may be regarded as a more physically grounded analogue of the supercluster model proposed over a quarter of a century ago.

The predicted increase in hole mass in the Cu-poor structures must also have practical ramifications. Heavier holes mean reduced mobility, which translates into a shorter hole diffusion length and, consequently, an increased photocarrier recombination rate. This is especially critical for n-type β-CIGSe, where holes are minority carriers. Since Shockley–Read–Hall recombination is typically limited by minority carrier diffusion, the increased hole mass – leading to reduced hole mobility – may constitute a fundamental obstacle to the application of β-CIGSe as an absorber in solar cells. In Cu-poor α-CIGSe, where holes are the majority carriers, reduced mobility may negatively affect conductivity, increasing series resistance and thereby lowering the fill factor of solar cells. How strong these adverse effects are and whether they can be offset by other factors in Cu-poor α-CIGSe is unclear. However, it is interesting to note that both the transport and recombination properties of stoichiometric α-CIGSe have been reported to exceed those of the Cu-poor absorber, whereas the latter is superior due to better interface quality (which reduces interfacial recombination) and lower doping density (which reduces tunnelling-assisted recombination).[2]

From a more fundamental standpoint, the increased and anisotropic hole mass exemplifies a carryover of structural anisotropy into the electronic property domain. This phenomenon is not uncommon, even in the field of thin-film photovoltaics, with two other cases being (i) low carrier masses along $(Sb_4S_6)_n$ ribbons in Sb_2S_3[116,117] and (ii) anisotropic transport in low-dimensional perovskite-inspired materials.[118] In this context, Cu-poor CIGSe stands out only because it exhibits emergent anisotropy – not strictly dictated by the crystallographic axes – that can be tuned by the orientation of the extended defect arrangements.

To our knowledge, off-stoichiometry-induced anisotropy in CIGSe has not yet been observed experimentally, presumably because it requires perfectly ordered crystals to manifest at the macroscale. In a partially disordered material, the effect is instead expected to reduce the overall carrier mobility for [Cu]/[III] < 1, as the contributions from different local environments average out. The isotropic change in mobility with off-stoichiometry has indeed been observed in epitaxial Cu-Ga-Se films[25] and Se-deficient CIGSe absorbers.[8] However, the available evidence is indirect and has alternative interpretations, such as increased scattering by defects[26] or changing the conductivity type.[8,11] The authors call for targeted experimental verification of the predicted evolution of hole mass in Cu-deficient CIGSe.

5. Summary

The computed evolution of electronic properties in the predicted topotactic ODC series for Cu-deficient CIGSe agrees well with prior experimental observations. The band gap widening upon Cu depletion seen in our calculations aligns perfectly with experimental literature values, within an error margin of ±0.1 eV. This result constitutes a huge improvement over earlier

computational works, especially for the Cu-Ga-Se system, and highlights the representativeness of the stable ODC structures analyzed herein. Our analysis confirms that the band gap change with off-stoichiometry originates from the reduced p-d antibonding in the valence band. Additionally, we demonstrate that Cu deficiency diminishes band dispersion at the valence band edge, impeding hole transport across thin Cu-poor regions in CIGSe. This change leads to anisotropic transport properties, although they may not manifest at the macroscopic scale due to partial cationic disorder. Instead, we propose that in the typical polycrystalline, partly disordered absorber films, the transport anisotropy is reflected in a reduction of the isotropic hole mobility, in agreement with prior measurements. While the full implications of our computational results for devices remain to be established, our presented findings firmly place the ODC continuum model as the most accurate representation of off-stoichiometry in CIGSe to date.

Conflicts of interest

There are no conflicts of interest to declare.

Data availability

The structures analyzed here have been deposited at the Materials Cloud Archive repository and can be accessed via the following identifier: https://doi.org/10.24435/materialscloud:j9-15.[44] Supplementary information (SI): complementary figures and tables. See DOI: https://doi.org/10.1039/d5ta07044a. Other raw data, processing scripts, and more detailed descriptions can be provided by the corresponding author upon reasonable request.

Acknowledgements

This work was partially supported by the Wallenberg Initiative Materials Science for Sustainability (WISE) funded by the Knut and Alice Wallenberg Foundation. The authors are also grateful for the financial support from the Swedish Foundation for Strategic Research (grant no. RMA15-0030) and the strategic research area STandUP for Energy. The computations and data handling were enabled by resources provided by the National Academic Infrastructure for Supercomputing in Sweden (NAISS), partially funded by the Swedish Research Council through grant agreement no. 2022-06725. The authors also thank Dr Jes K. Larsen and Dr Oleksandr I. Malyi for the insightful scientific discussions.

References

1 J. Keller, K. Kiselman, O. Donzel-Gargand, N. M. Martin, M. Babucci, O. Lundberg, E. Wallin, L. Stolt and M. Edoff, *Nat. Energy*, 2024, **9**, 467–478.
2 S. Siebentritt, L. Gütay, D. Regesch, Y. Aida and V. Deprédurand, *Sol. Energy Mater. Sol. Cells*, 2013, **119**, 18–25.
3 K. V. Sopiha, J. Keller, C. Persson, J. J. S. Scragg, C. Platzer-Björkman and M. Edoff, *J. Mater. Chem. A*, 2026, DOI: 10.1039/d5ta07043k.
4 D. Schmid, M. Ruckh, F. Grunwald and H. W. Schock, *J. Appl. Phys.*, 1993, **73**, 2902–2909.
5 R. R. Philip and B. Pradeep, *Semicond. Sci. Technol.*, 2003, **18**, 768.
6 R. Márquez and C. Rincón, *Sol. Energy Mater. Sol. Cells*, 2002, **71**, 19–26.
7 R. Jacob, R. Geethu, T. Shripathi, G. S. Okram, V. Ganesan, B. Pradeep, K. S. Urmila and R. R. Philip, *Phys. Status Solidi A*, 2012, **209**, 2195–2200.
8 L. Sun, J. Ma, N. Yao, Z. Huang and J. Chu, *J. Mater. Sci.: Mater. Electron.*, 2016, **27**, 9124–9130.
9 S. Kohiki, M. Nishitani, T. Negami and T. Wada, *Phys. Rev. B*, 1992, **45**, 9163–9168.
10 Y. B. K. Reddy and V. S. Raja, *Mater. Lett.*, 2004, **58**, 1839–1843.
11 A. V. Mudryi, T. V. Tavrina and E. I. Rogacheva, *Inorg. Mater.*, 2007, **43**, 926–930.
12 L. Durán, C. Guerrero, E. Hernández, J. M. Delgado, J. Contreras, S. M. Wasim and C. A. Durante Rincón, *J. Phys. Chem. Solids*, 2003, **64**, 1907–1910.
13 S. M. Wasim, C. Rincón and G. Marín, *Phys. Status Solidi A*, 2002, **194**, 244–252.
14 A. Sharan, F. P. Sabino, A. Janotti, N. Gaillard, T. Ogitsu and J. B. Varley, *J. Appl. Phys.*, 2020, **127**, 065303.
15 E. Ghorbani, J. Kiss, H. Mirhosseini, G. Roma, M. Schmidt, J. Windeln, T. D. Kühne and C. Felser, *J. Phys. Chem. C*, 2015, **119**, 25197–25203.
16 H. Xiao and W. A. Goddard, *J. Chem. Phys.*, 2014, **141**, 094701.
17 T. Maeda, W. Gong and T. Wada, *Jpn. J. Appl. Phys.*, 2016, **55**, 04ES15.
18 S. B. Zhang, S.-H. Wei, A. Zunger and H. Katayama-Yoshida, *Phys. Rev. B*, 1998, **57**, 9642–9656.
19 S. Kumar, S. Joshi and S. Auluck, *Mater. Chem. Phys.*, 2015, **162**, 372–379.
20 H. Zhao, M. Kumar and C. Persson, *Phys. Status Solidi C*, 2012, **9**, 1600–1603.
21 W. Liu, H. Liang, Y. Duan and Z. Wu, *Phys. Rev. Mater.*, 2019, **3**, 125405.
22 E. Ghorbani, P. Erhart and K. Albe, *Phys. Rev. Mater.*, 2019, **3**, 075401.
23 A. Hofmann and C. Pettenkofer, *Appl. Phys. Lett.*, 2012, **101**, 062108.
24 K. Ueda, T. Maeda and T. Wada, *Thin Solid Films*, 2017, **633**, 23–30.
25 A. Gerhard, W. Harneit, S. Brehme, A. Bauknecht, U. Fiedeler, M. Ch. Lux-Steiner and S. Siebentritt, *Thin Solid Films*, 2001, **387**, 67–70.
26 C. Rincón, S. M. Wasim and G. Marín, *Appl. Phys. Lett.*, 2002, **80**, 998–1000.
27 G. Kresse and J. Furthmüller, *Phys. Rev. B*, 1996, **54**, 11169–11186.
28 G. Kresse and D. Joubert, *Phys. Rev. B*, 1999, **59**, 1758–1775.

29 J. P. Perdew, K. Burke and M. Ernzerhof, *Phys. Rev. Lett.*, 1996, **77**, 3865–3868.
30 S. L. Dudarev, G. A. Botton, S. Y. Savrasov, C. J. Humphreys and A. P. Sutton, *Phys. Rev. B*, 1998, **57**, 1505–1509.
31 F. Tran and P. Blaha, *Phys. Rev. Lett.*, 2009, **102**, 226401.
32 A. V. Krukau, O. A. Vydrov, A. F. Izmaylov and G. E. Scuseria, *J. Chem. Phys.*, 2006, **125**, 224106.
33 J. P. Perdew, A. Ruzsinszky, G. I. Csonka, O. A. Vydrov, G. E. Scuseria, L. A. Constantin, X. Zhou and K. Burke, *Phys. Rev. Lett.*, 2008, **100**, 136406.
34 J. Sun, A. Ruzsinszky and J. P. Perdew, *Phys. Rev. Lett.*, 2015, **115**, 036402.
35 R. Cherian, P. Mahadevan and C. Persson, *Solid State Commun.*, 2009, **149**, 1810–1813.
36 W. Setyawan and S. Curtarolo, *Comput. Mater. Sci.*, 2010, **49**, 299–312.
37 R. Chen and C. Persson, *J. Appl. Phys.*, 2012, **112**, 103708.
38 C. Persson, *Appl. Phys. Lett.*, 2008, **93**, 072106.
39 R. Chen and C. Persson, *Thin Solid Films*, 2011, **519**, 7503–7507.
40 S. P. Ong, W. D. Richards, A. Jain, G. Hautier, M. Kocher, S. Cholia, D. Gunter, V. L. Chevrier, K. A. Persson and G. Ceder, *Comput. Mater. Sci.*, 2013, **68**, 314–319.
41 K. Momma and F. Izumi, *J. Appl. Crystallogr.*, 2011, **44**, 1272–1276.
42 A. M. Ganose, A. Searle, A. Jain and S. M. Griffin, *J. Open Source Softw.*, 2021, **6**, 3089.
43 G. K. H. Madsen, J. Carrete and M. J. Verstraete, *Comput. Phys. Commun.*, 2018, **231**, 140–145.
44 K. Sopiha, J. Keller, C. Persson, J. Scragg, C. Platzer-Björkman and M. Edoff, *Functional off-stoichiometry in Cu(In,Ga)Se2*, Materials Cloud Archive, 2025, 2025.134, DOI: 10.24435/materialscloud:j9-15.
45 S. M. Wasim, C. Rincón, G. Marín and J. M. Delgado, *Appl. Phys. Lett.*, 2000, **77**, 94–96.
46 G. Marín, S. M. Wasim, C. Rincón, G. Sánchez Pérez, Ch. Power and A. E. Mora, *J. Appl. Phys.*, 1998, **83**, 3364–3366.
47 C. Rincón, S. M. Wasim, G. Marín and I. Molina, *J. Appl. Phys.*, 2002, **93**, 780–782.
48 G. Marín, S. Tauleigne, S. M. Wasim, R. Guevara, J. M. Delgado, C. Rincón, A. E. Mora and G. Perez, *Mater. Res. Bull.*, 1998, **33**, 1057–1068.
49 C.-D. Kim, M.-S. Jin and W.-T. Kim, *J. Korean Phys. Soc.*, 1998, **32**, 750.
50 T. Negami, N. Kohara, M. Nishitani, T. Wada and T. Hirao, *Appl. Phys. Lett.*, 1995, **67**, 825–827.
51 M. León, R. Serna, S. Levcenko, A. Nateprov, A. Nicorici, J. M. Merino and E. Arushanov, *J. Appl. Phys.*, 2007, **101**, 013524.
52 M. León, R. Serna, S. Levcenko, A. Nateprov, A. Nicorici, J. M. Merino and E. Arushanov, *Phys. Status Solidi A*, 2006, **203**, 2913–2918.
53 M. A. Contreras, L. M. Mansfield, B. Egaas, J. Li, M. Romero, R. Noufi, E. Rudiger-Voigt and W. Mannstadt, *Prog. Photovoltaics Res. Appl.*, 2012, **20**, 843–850.
54 M. I. Alonso, K. Wakita, J. Pascual, M. Garriga and N. Yamamoto, *Phys. Rev. B*, 2001, **63**, 075203.
55 S. Levcenko, N. N. Syrbu, E. Arushanov, V. Tezlevan, R. Fernández-Ruiz, J. M. Merino and M. León, *J. Appl. Phys.*, 2006, **99**, 073513.
56 E. J. Friedrich, J. F. Trigo, J. Ramiro, C. Guillén, J. M. Merino and M. León, *J. Phys. D: Appl. Phys.*, 2009, **42**, 085401.
57 G. El haj Moussa Ariswan, M. Abdelali, F. Guastavino and C. Llinares, *Solid State Commun.*, 2002, **124**, 391–396.
58 E. Hernández, L. Durán, C. A. Durante Rincón, G. Aranguren, C. Guerrero and J. Naranjo, *Cryst. Res. Technol.*, 2002, **37**, 1227–1233.
59 G. Marín, C. Rincón, S. M. Wasim, G. Sánchez Pérez and I. Molina, *J. Alloys Compd.*, 1999, **283**, 1–4.
60 J. L. Shay and B. Tell, *Surf. Sci.*, 1973, **37**, 748–762.
61 S. Levcenko, N. N. Syrbu, A. Nateprov, E. Arushanov, J. M. Merino and M. León, *J. Phys. D: Appl. Phys.*, 2006, **39**, 1515.
62 J. P. Perdew and M. Levy, *Phys. Rev. Lett.*, 1983, **51**, 1884–1887.
63 M. K. Y. Chan and G. Ceder, *Phys. Rev. Lett.*, 2010, **105**, 196403.
64 J. K. Larsen, K. V. Sopiha, C. Persson, C. Platzer-Björkman and M. Edoff, *Adv. Sci.*, 2022, **9**, 2200848.
65 K. Park, B.-H. Jeong, H. Y. Lim and J.-S. Park, *J. Appl. Phys.*, 2021, **129**, 025703.
66 M. Malitckaya, T. Kunze, H.-P. Komsa, V. Havu, E. Handick, R. G. Wilks, M. Bär and M. J. Puska, *ACS Appl. Mater. Interfaces*, 2019, **11**, 3024–3033.
67 C.-H. Chang, S.-H. Wei, J. W. Johnson, S. B. Zhang, N. Leyarovska, G. Bunker and T. J. Anderson, *Phys. Rev. B*, 2003, **68**, 054108.
68 X. Chen, W. Liu and Y. Duan, *J. Phys.: Condens. Matter*, 2020, **33**, 075401.
69 M. Yarema, N. Yazdani, O. Yarema, N. Đorđević, W. M. M. Lin, D. Bozyigit, S. Volk, A. Moser, A. Turrini, P. A. Khomyakov, M. Nachtegaal, M. Luisier and V. Wood, *Adv. Mater.*, 2024, **36**, 2406351.
70 C. D. R. Ludwig, T. Gruhn, C. Felser and J. Windeln, *Phys. Rev. B*, 2011, **83**, 174112.
71 A. Moser, O. Yarema, N. Rusch, N. Đorđević, W. M. M. Lin, D. Bozyigit, N. Yazdani, M. Yarema, M. Luisier and V. Wood, *ACS Nanosci. Au*, 2024, **5**, 21–28.
72 F. Jiang and J. Feng, *Appl. Phys. Lett.*, 2006, **89**, 221920.
73 J. Kiss, T. Gruhn, G. Roma and C. Felser, *J. Phys. Chem. C*, 2013, **117**, 10892–10900.
74 J. Kiss, T. Gruhn, G. Roma and C. Felser, *J. Phys. Chem. C*, 2013, **117**, 25933–25938.
75 J. Pohl and K. Albe, *Phys. Rev. B*, 2013, **87**, 245203.
76 S. B. Zhang, S.-H. Wei and A. Zunger, *Phys. Rev. Lett.*, 1997, **78**, 4059–4062.
77 L.-H. Tu, N. T. T. Tran, S.-K. Lin and C.-H. Lai, *Adv. Energy Mater.*, 2023, **13**, 2301227.
78 M. Hellenbrandt, *Crystallogr. Rev.*, 2004, **10**, 17–22.
79 A. Jain, S. P. Ong, G. Hautier, W. Chen, W. D. Richards, S. Dacek, S. Cholia, D. Gunter, D. Skinner, G. Ceder and K. A. Persson, *APL Mater.*, 2013, **1**, 011002.

80 S. Kirklin, J. E. Saal, B. Meredig, A. Thompson, J. W. Doak, M. Aykol, S. Rühl and C. Wolverton, *npj Comput. Mater.*, 2015, **1**, 1–15.
81 J. K. Larsen, O. Donzel-Gargand, K. V. Sopiha, J. Keller, K. Lindgren, C. Platzer-Björkman and M. Edoff, *ACS Appl. Energy Mater.*, 2021, **4**, 1805–1814.
82 J. E. Jaffe and A. Zunger, *Phys. Rev. B*, 1984, **29**, 1882–1906.
83 C. Persson, *Braz. J. Phys.*, 2006, **36**, 948–951.
84 S. Minoura, K. Kodera, T. Maekawa, K. Miyazaki, S. Niki and H. Fujiwara, *J. Appl. Phys.*, 2013, **113**, 063505.
85 T. Maeda and T. Wada, *Jpn. J. Appl. Phys.*, 2010, **49**, 04DP07.
86 A. Zakutayev, C. M. Caskey, A. N. Fioretti, D. S. Ginley, J. Vidal, V. Stevanovic, E. Tea and S. Lany, *J. Phys. Chem. Lett.*, 2014, **5**, 1117–1125.
87 M. Souilah, A. Lafond, C. Guillot-Deudon, S. Harel and M. Evain, *J. Solid State Chem.*, 2010, **183**, 2274–2280.
88 A. Stokes, M. Al-Jassim, A. Norman, D. Diercks, B. Gorman and P. Photovolt, *Prog. Photovoltaics Res. Appl.*, 2017, **25**, 764–772.
89 S. Wei and A. Zunger, *J. Appl. Phys.*, 1995, **78**, 3846–3856.
90 J. Keller, K. V. Sopiha, O. Stolt, L. Stolt, C. Persson, J. J. S. Scragg, T. Törndahl and M. Edoff, *Prog. Photovoltaics Res. Appl.*, 2020, **28**, 237–250.
91 Y.-S. Kim, M. Marsman, G. Kresse, F. Tran and P. Blaha, *Phys. Rev. B*, 2010, **82**, 205212.
92 Y. Zhang, Y. Wang, L. Xi, R. Qiu, X. Shi, P. Zhang and W. Zhang, *J. Chem. Phys.*, 2014, **140**, 074702.
93 R. R. Philip, S. Dhanya, T. Namitha Ashokan and B. Pradeep, *J. Phys. Chem. Solids*, 2011, **72**, 294–298.
94 P. Malar and S. Kasiviswanathan, *Sol. Energy Mater. Sol. Cells*, 2005, **85**, 521–533.
95 E. Arushanov, L. Kulyuk, O. Kulikova, V. Tezlevan, R. F. Ruiz and M. León, *J. Phys. D: Appl. Phys.*, 2001, **34**, 3480–3484.
96 B. Zhu, S. R. Kavanagh and D. Scanlon, *J. Open Source Softw.*, 2024, **9**, 5974.
97 M. V. Yakushev, F. Luckert, A. V. Rodina, C. Faugeras, A. V. Karotki, A. V. Mudryi and R. W. Martin, *Appl. Phys. Lett.*, 2012, **101**, 262101.
98 M. V. Yakushev, A. V. Rodina, R. P. Seisyan, Yu. E. Kitaev, S. A. Vaganov, M. A. Abdullaev, A. V. Mudryi, T. V. Kuznetsova, C. Faugeras and R. W. Martin, *Phys. Rev. B*, 2019, **100**, 235202.
99 C. Persson and A. Zunger, *Phys. Rev. Lett.*, 2003, **91**, 266401.
100 I. Matsuda and S. Hasegawa, *J. Phys.: Condens. Matter*, 2007, **19**, 355007.
101 S. Ishizuka and P. J. Fons, *Phys. Rev. Appl.*, 2021, **15**, 054005.
102 S. Ji, T. Hayakawa, N. Suyama, K. Nakada and A. Yamada, *Jpn. J. Appl. Phys.*, 2020, **59**, 041003.
103 T. Nishimura, K. Nakada and A. Yamada, *ACS Appl. Energy Mater.*, 2019, **2**, 5103–5108.
104 J. Keller, N. Martin, O. Donzel-Gargand, K. Kiselman, U. Zimmermann, L. Stolt, C. Platzer-Björkman and M. Edoff, *Sol. RRL*, 2024, **8**, 2301018.
105 J. Keller, L. Stolt, K. V. Sopiha, J. K. Larsen, L. Riekehr and M. Edoff, *Sol. RRL*, 2020, **4**, 2000508.
106 J. Keller, P. Pearson, N. Shariati Nilsson, O. Stolt, L. Stolt and M. Edoff, *Sol. RRL*, 2021, **5**, 2100403.
107 S. Ishizuka, A. Yamada, P. J. Fons, Y. Kamikawa-Shimizu, H. Komaki, H. Shibata and S. Niki, *Appl. Phys. Lett.*, 2014, **104**, 031606.
108 J. Keller, O. V. Bilousov, E. Wallin, O. Lundberg, J. Neerken, S. Heise, L. Riekehr, M. Edoff and C. Platzer-Björkman, *Phys. Status Solidi A*, 2019, **216**, 1900472.
109 T. Ogihara, A. Sadono, T. Nishimura, K. Nakada and A. Yamada, *Jpn. J. Appl. Phys.*, 2017, **56**, 062301.
110 C. Insignares-Cuello, C. Broussillou, V. Bermúdez, E. Saucedo, A. Pérez-Rodríguez and V. Izquierdo-Roca, *Appl. Phys. Lett.*, 2014, **105**, 021905.
111 K. V. Sopiha, J. K. Larsen, O. Donzel-Gargand, F. Khavari, J. Keller, M. Edoff, C. Platzer-Björkman, C. Persson and J. J. Scragg, *J. Mater. Chem. A*, 2020, **8**, 8740–8751.
112 T. Nakada, D. Iga, H. Ohbo and A. Kunioka, *Jpn. J. Appl. Phys.*, 1997, **36**, 732–737.
113 J. H. Kim, S. T. Kim, L. Larina, B. T. Ahn, K. Kim and J. H. Yun, *Sol. Energy Mater. Sol. Cells*, 2018, **179**, 289–296.
114 J. Keller, H. Aboulfadl, L. Stolt, O. Donzel-Gargand and M. Edoff, *Sol. RRL*, 2022, **6**, 2200044.
115 A. Rockett, *Thin Solid Films*, 2000, **361–362**, 330–337.
116 R. Kondrotas, C. Chen and J. Tang, *Joule*, 2018, **2**, 857–878.
117 X. Wang, Z. Li, S. R. Kavanagh, A. M. Ganose and A. Walsh, *Phys. Chem. Chem. Phys.*, 2022, **24**, 7195–7202.
118 Y.-T. Huang, S. R. Kavanagh, D. O. Scanlon, A. Walsh and R. L. Z. Hoye, *Nanotechnology*, 2021, **32**, 132004.